PHYSICAL REVIEW A **100**, 022507 (2019)

Observing pre-edge *K*-shell resonances in Kr, Xe, and XeF$_2$

S. H. Southworth,[1] R. W. Dunford,[1] D. Ray,[1,*] E. P. Kanter,[1] G. Doumy,[1] A. M. March,[1] P. J. Ho,[1] B. Krässig,[1,†] Y. Gao,[1,‡]
C. S. Lehmann,[1,§] A. Picón,[1,∥] L. Young,[1,2] D. A. Walko,[3] and L. Cheng[4]
[1] *Chemical Sciences and Engineering Division, Argonne National Laboratory, Lemont, Illinois 60439, USA*
[2] *The James Franck Institute and Department of Physics, The University of Chicago, Chicago, Illinois 60637, USA*
[3] *Advanced Photon Source, Argonne National Laboratory, Lemont, Illinois 60439, USA*
[4] *Department of Chemistry, Johns Hopkins University, Baltimore, Maryland 21218, USA*

(Received 13 May 2019; published 9 August 2019)

The $1s \rightarrow np$ Rydberg transitions below the $1s$ ionization thresholds of Kr and Xe are obscured in x-ray absorption spectra due to core-hole lifetime broadening. However, the np spectator electrons associated with those resonances can affect the core-hole decay spectra. We report on ion charge-state distributions of Kr and Xe measured in coincidence with $KL_{2,3}$ ($K\alpha_{1,2}$), $KM_{2,3}$ ($K\beta_{1,3}$), and $\mathrm{KN}_{2,3}$ ($K\beta_2$) x-ray fluorescence as the incident x-ray energy is scanned through pre-edge resonances and ionization thresholds. The coincidence measurements select vacancy cascades that begin with a radiative transition that transfers $1s$ holes to the $2p$, $3p$, and $4p$ shells followed by emission of Auger electrons. We observe shifts of ion yields from higher to lower charge states that we attribute to np spectator electrons. For the special case of Kr^{1+} that is produced in coincidence with $K\beta_2$ x rays, the ion yield decreases in the pre-edge region. This is attributed to production of neutral, metastable Kr $4p^{-1}np$ states that reduce the Kr^{1+} yield. Model fits to the x-ray absorption spectra are presented to show the lifetime broadened pre-edge resonances and ionization thresholds. High-level relativistic coupled-cluster calculations that treat relativistic, electron correlation, and wave function relaxation effects on the same footing obtain agreement with the experimental $1s$ ionization energies of Kr and Xe to <2 eV. The Xe K-edge x-ray absorption spectrum and ion charge-state distributions of XeF$_2$ were also recorded. Excitation of the $7\sigma_u$ lowest unoccupied molecular orbital (LUMO) in XeF$_2$ is observed in the pre-edge region. Our *ab initio* calculations find that the $6p_z$ Rydberg state is strongly perturbed by the presence of the $7\sigma_u$ LUMO. A fit to the measured LUMO, $6p_x$, $6p_y$, $6p_z$ Rydberg states, and ionization threshold is guided by the relativistic coupled-cluster calculations. The F ligands modify the valence electron charge distribution and result in a $\sim$2.3 eV chemical shift of the Xe $1s$ ionization energy relative to atomic Xe. Xe $1s^{-1}$ core-hole decay in XeF$_2$ results in ionization of the F ligands and energetic fragmentation into atomic ions. Ion charge-state spectra of XeF$_2$ were recorded in coincidence with x-ray fluorescence for excitation on the LUMO resonance and above the Xe $1s$ ionization threshold. For the ion time of flight spectra recorded on the LUMO resonance, the F^{q+} ($q = 1$–4) peaks are split into two peaks along the linear polarization direction of the incident x-ray beam. This effect is attributed to spatial alignment of XeF$_2$ molecules by resonant x-ray absorption, and the peak splittings are used to measure the F ion fragmentation energies following $K\alpha_{1,2}$, $K\beta_{1,3}$, and $K\beta_2$ x-ray fluorescence. We observe variations of the F ion charge state yields and fragmentation energies for the three fluorescence pathways that leave the molecule in different outer-shell hole states.

DOI: 10.1103/PhysRevA.100.022507

I. INTRODUCTION

It is well established that photoionization and core-hole decay of inner-shell electrons near threshold exhibit phenomena that require a theoretical description in which the photoionization and core-hole decay are treated as a single quantum process referred to as resonant Raman scattering [1–5]. In radiationless decay, post-collision interaction (PCI) among the photoelectron, Auger electron, and nascent atomic ion results in energy exchanges between the two continuum electrons and even recapture of slow photoelectrons into Rydberg states [6–8]. Radiative decay in the near threshold region is referred to as resonant inelastic x-ray scattering (RIXS) and couples the resonant core-excited and final states [9–11]. High-resolution RIXS can be used to obtain electronic and structural information on transition metal complexes [12] and on excitations in complex materials [13].

Observing resonance and threshold effects at the K edges of heavier atoms is hampered by lifetime broadening of the $1s^{-1}$ core holes that obscures pre-edge resonance structure. As the core-hole width increases, the $1s \rightarrow np$ Rydberg

---

[*] Present address: KLA Corporation, Milpitas, California 95035, USA.

[†] Present address: 437 7th Avenue, La Grange, Illinois 60525, USA.

[‡] Present address: National Synchrotron Light Source II, Brookhaven National Laboratory, Upton, New York 11973, USA.

[§] Present address: Fachbereich Chemie, Philipps-Universität Marburg, Marburg, Germany.

[∥] Present address: Department of Chemistry, Universidad Autónoma de Madrid, Madrid, Spain.

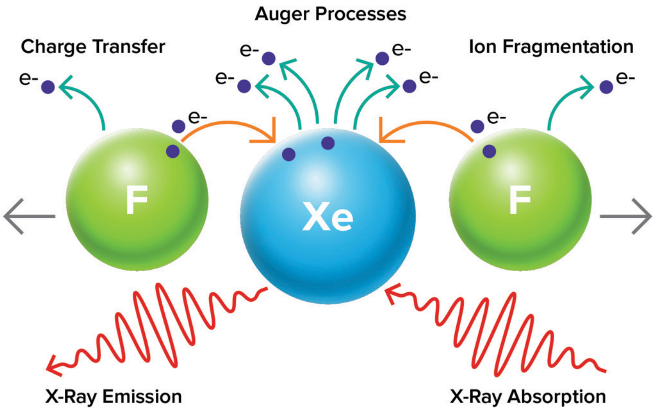

FIG. 1. Illustration of inner-shell photoionization and core-hole decay processes in XeF_2 molecules. X-ray absorption ejects a $1s$ electron from the Xe atom. The present experiments select core-hole decay processes that begin with an x-ray emission step that transfers the $1s$ hole to $2p$, $3p$, or $4p$ holes. Series of Auger decays from those hole states lead to ranges of final charge states. Auger decays involving delocalized orbitals and charge transfer from Xe to the F sites spreads charge across the molecule. The molecular ion is unstable due to Coulomb repulsion and dissociates into energetic atomic ions.

transitions become less visible as shown in the x-ray absorption spectra of Ne, Ar, Kr, and Xe [14–17] for which the K-hole level widths (in eV) are 0.27, 0.656, 2.714, and 11.49, respectively [14,18]. One way to observe pre-edge resonances despite lifetime broadening is to combine high-resolution x-ray absorption and x-ray emission spectroscopies to record RIXS scans [2,12,19]. Coincidence measurements among the ejected electrons, photons, and ions help to unravel complex core-hole decay pathways, as demonstrated in a recent study of Ar K-shell photoionization [20]. In the present work, our goal is to observe effects of pre-edge K-shell resonances on core-hole decay measurements in Kr, Xe, and XeF_2. We use a high-resolution x-ray beamline to tune the incident photon energy across the pre-edge and threshold regions and x-ray/ion coincidence spectroscopy to select decay pathways that begin with a radiative transition followed by series of Auger transitions that produce ion charge states. In Kr and Xe, we explore the effects on charge state distributions of spectator electrons associated with $1s \rightarrow np$ transitions. In XeF_2, decay of Xe $1s$ hole states leads to ionization of the F ligands, charge spreads across the molecule, and it dissociates into three atomic ions. Figure 1 illustrates the processes involved, i.e., x-ray absorption, x-ray emission, Auger decays, charge transfer, and ion fragmentation. The present work extends earlier x-ray/ion coincidence studies of Kr [21,22] and another of Xe and XeF_2 that focused on charge production, charge distribution, and the effects of interatomic Coulomb decay [23]. The present results were recorded with an improved apparatus and focus on pre-edge resonances in the atoms and molecule. The measurements are supported by high-level *ab initio* relativistic calculations of inner-shell excitation and ionization energies and transition strengths.

The physics of core-hole decays has practical significance to understanding mechanisms of x-ray damage in molecules and materials. Also, the therapeutic effects of energetic photoelectrons and Auger electrons from x-ray ionization of heavy atoms injected into tumors are being investigated in medical radiotherapy applications [24,25]. In recent years, a new chapter has opened in studies of inner-shell photoionization with the use of intense, femtosecond x-ray pulses that interact nonlinearly with atoms and molecules by sequential absorption of multiple photons in competition with core-hole decays [26–29]. Recent theoretical work on calculating ionization dynamics in the ultraintense x-ray regime have focused attention on resonance and relativistic interactions [30,31]. The experiments discussed here use single x-ray photoionization of heavy atoms with an emphasis on pre-edge resonances and near-threshold ionization. Obtaining accurate electronic structures and transition strengths to calculate x-ray absorption spectra of molecules remains a formidable challenge [32]. Here we employ equation-of-motion coupled cluster (EOM-CC) methods [33–37] within the core-valence separation (CVS) scheme [38,39]. The CVS-EOM-CC methods have recently been shown to yield highly accurate results for $1s$ ionization energies of the second-row elements [40]. Using the CVS-EOM-CC methods together with relativistic Hamiltonians [41], we have calculated the Kr $1s$ ionization energy in Kr and the Xe $1s$ ionization energies in Xe and XeF_2. We have also calculated the excitation energies and oscillator strengths of the $1s \rightarrow 7\sigma_u$ lowest unoccupied molecular orbital (LUMO) and $1s \rightarrow 6p_x, 6p_y, 6p_z$ Rydberg states in XeF_2.

Section II of this paper describes the x-ray absorption and x-ray/ion coincidence instruments and methods. Section III presents the theoretical considerations, computational methods, and results. The measurements and comparisons with theory are discussed in Sec. IV and conclusions are given in Sec. V.

II. EXPERIMENTAL METHODS

The experiments were performed at beamline 7-ID of Argonne's Advanced Photon Source (APS) [42]. For Kr K-edge measurements near 14 keV, the undulator's 3rd harmonic was used with the 111 reflection of the diamond double-crystal monochromator. For Xe and XeF_2 K-edge measurements near 34 keV, the undulator's 5th harmonic was used with the diamond 333 reflection. For the 34 keV measurements, a thin copper filter reduced low-energy x rays from the 111 reflection. The estimated bandwidths at both Kr and Xe edges were $\lesssim 1$ eV. The energy scales were referenced to the Kr $1s$ ionization energy of 14327.19 (13) eV and Xe $1s$ ionization energy of 34565.13 (33) eV [43]. Using horizontal and vertical slits, the x-ray beam size on target was <1 mm^2. The x-ray/ion coincidence instrument was an improved version of the setup used previously [23]. The ion time-of-flight (TOF) instrument has a larger number and larger size of ion extraction and acceleration elements and a longer drift tube. This gives a more versatile instrument with increased mass/charge resolution and better collection of energetic fragment ions. Static potentials are placed on the ion optical elements and the ions are detected with microchannel plates. The Ge x-ray fluorescence spectrometer used in Ref. [23] was replaced by a SiLi detector having better resolution but decreased

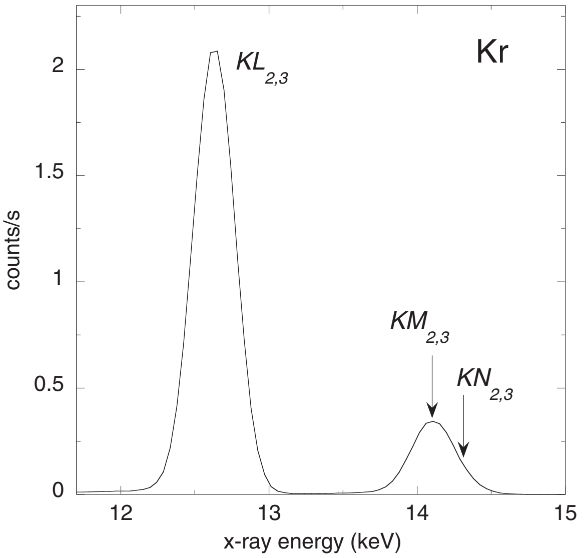

FIG. 2. X-ray emission spectrum of Kr measured with a SiLi detector. The energies and relative intensities of the $KL_{2,3}$ ($K\alpha_{1,2}$), $KM_{2,3}$ ($K\beta_{1,3}$), and $\mathrm{KN}_{2,3}$ ($K\beta_2$) transitions are listed in Table I.

efficiency at higher x-ray energies. The SiLi detector and ion spectrometer are positioned opposite each other with the x-ray beam and effusive gas jet between. The flight axis of the TOF spectrometer is along the x-ray linear polarization direction. An event-mode data acquisition system recorded the fluorescent x rays and ions in coincidence. For the molecular target, multiple fragment ions were measured in coincidence with the x-ray fluorescence. Events were triggered by detection of a fluorescent x ray. To improve the ion TOF resolution, the SiLi pulses were referenced to the RF clock of the storage ring. The storage ring contained 24 electron bunches spaced by 153 ns with a total current of 102 mA. A wait time following a trigger pulse from the SiLi detector allowed the ion TOFs to be in the μs range for high resolution. The isotopic structures of Kr and Xe were resolved in the ion spectra. In the case of $\mathrm{XeF_2}$, the F ion peaks are broadened by energetic dissociation of the molecular ion as illustrated in Fig. 1. The ion times of flight can be accurately calculated using the geometry and electric fields of the instrument. The TOF calculations were used to determine the F ion fragmentation energies.

The x-ray emission spectra (XES) of Kr, Xe, and $\mathrm{XeF_2}$ recorded with the SiLi detector are plotted in Figs. 2 and 3. The XES of Xe and $\mathrm{XeF_2}$ overlap within the resolution of the detector and their sum is plotted in Fig. 3. The energies and relative intensities of the XES transitions taken from Ref. [44] are listed in Table I. The experiments select core-hole decays that begin with a radiative step that transfers the 1s holes to a 2p, 3p, or 4p hole. Sequences of Auger decays from those hole states lead to ranges of final charge states. In the $\mathrm{XeF_2}$ case, Auger decays from delocalized orbitals and charge transfer from Xe to the F ligands spreads charge across the molecule and it dissociates [23,45,46]. To obtain ion spectra in coincidence with particular XES transitions, the event files were analyzed with filters on selected x-ray energy ranges.

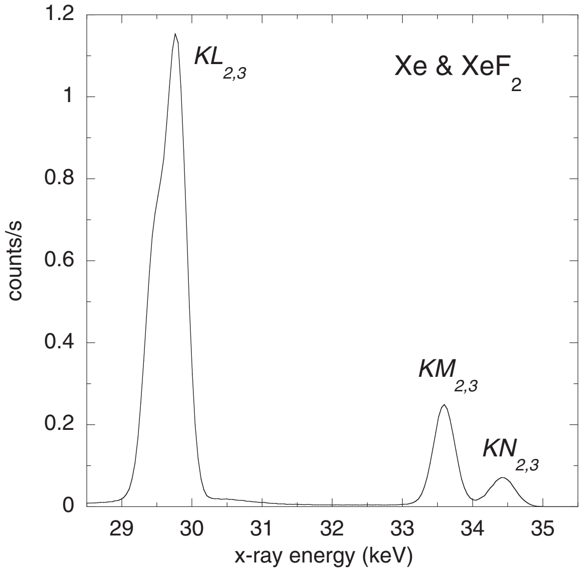

FIG. 3. X-ray emission spectrum of Xe and $\mathrm{XeF_2}$ measured with a SiLi detector. The Xe and $\mathrm{XeF_2}$ spectra overlap and their sum is plotted. The energies and relative intensities of the $KL_{2,3}$ ($K\alpha_{1,2}$), $KM_{2,3}$ ($K\beta_{1,3}$), and $\mathrm{KN}_{2,3}$ ($K\beta_2$) transitions are listed in Table I.

III. THEORY

It is a challenging task to obtain computational results that are sufficiently accurate to facilitate or even guide the experimental analysis; the scale of the Xe 1s ionization or excitation energies is as large as 34 keV, whereas the relative shifts that are targeted range from a few to 10 eV and constitute only a very small fraction of the total ionization or excitation energies. The first challenge to address is the treatment of strong relaxation of wave functions induced by the removal of a deep inner-shell electron. We have based our calculations on the core-valence-separated equation-of-motion coupled-cluster (CVS-EOM-CC) methods [39], which feature systematic improvements for the treatment of electron correlation and wave function relaxation. In particular, the convergence of the computed results with respect to the excitation rank can serve to assess the accuracy of the results. It has been shown recently that the errors of CVS-EOM-CC singles, doubles and triples (CCSDT) results for the *K*-edge ionization energies of second-row elements are less than 0.5 eV [40]. The present study aims to extend the calculations to heavy elements. The

TABLE I. Energies and relative intensities of x-ray emission lines of Kr and Xe taken from Ref. [44].

	Kr		Xe	
Line	Energy (eV)	Relative intensity (%)	Energy (eV)	Relative intensity (%)
$K\alpha_2$	12598	52	29458	54
$K\alpha_1$	12649	100	29779	100
$K\beta_3$	14104	7	33562	9
$K\beta_1$	14112	14	33624	18
$K\beta_2$	14315	2	34415	5

large-scale CVS-EOM-CCSDT calculations presented here are enabled by the efficient implementation of the CCSDT and EOM-CCSDT methods by Matthews *et al.* [47,48] in the CFOUR program package [49].

The other major challenge to address in the calculation of Kr and Xe K-edge ionization and excitation energies and spectra is the treatment of strong relativistic effects on the Kr and Xe $1s$ electrons, in which the scalar relativistic effects are dominating and the second-order spin-orbit (SO) effects are relatively small corrections. Considering the computational costs, the scalar-relativistic two-component EOM-CC calculations are as efficient as the corresponding nonrelativistic ones, while the inclusion of SOC in CC calculations is computationally demanding due to spin-symmetry breaking. Therefore, we have adopted a cost-effective scheme consisting of a thorough treatment of the large and computationally cheap scalar-relativistic effects using highly accurate EOM-CC wave functions and an approximate treatment of the small and expensive SOC effects. Such a treatment is possible with the rigorous spin-separation scheme for the Dirac-Coulomb (DC) Hamiltonian, which leads to the spin-free four-component DC (SFDC) approach [50]. Further, since the positronic solutions of the Dirac equation [41] are of no relevance, the computational efficiency is further enhanced by using the spin-free exact two-component theory in its one-electron variant (SFX2C-1e) [51]. The SFX2C-1e scheme decouples the electronic and positronic degrees of freedom in the one-electron Dirac Hamiltonian in its matrix representation [52–55]. The combination of the "electrons-only" one-electron Hamiltonian with the untransformed two-electron Coulomb interaction in the SFX2C-1e scheme leads to both the prominent computational advantage of involving only the nonrelativistic two-electron integrals and the underlying approximations of the neglect of the "two-electron picture change" (2e-pc) effects [56] in comparison to the SFDC approach. The SFDC and SFX2C-1e calculations presented here are enabled by the efficient implementation of these relativistic quantum-chemical methods in the CFOUR program [57,58]. Finally, the Breit term and quantum electrodynamics (QED) effects make important contributions to the Kr and Xe $1s$ orbital energies [59,60] and will also be considered.

Based on the above considerations, for the Kr $1s$ ionization energy in Kr and the Xe $1s$ ionization energies in Xe and $\mathrm{XeF_2}$, we have performed SFX2C-1e-CVS-EOM-CCSD and CCSDT calculations with the uncontracted ANO-RCC (ANO-RCC-unc) basis sets [61,62], except that the uncontracted cc-pVTZ (cc-pVTZ-unc) basis set [63] was used for F in the CCSDT calculation. The 2e-pc corrections have been obtained as the difference between the SFDC-EOM-CCSD/ANO-RCC-unc and SFX2C-1e-EOM-CCSD/ANO-RCC-unc results. The much smaller second-order spin-orbit corrections within the DC Hamiltonian have been obtained as the difference between X2CAMF [64] and SFX2C-1e Hartree-Fock orbital energies using the ANO-RCC-unc basis sets. The contributions of the Breit term and the QED effects (these two are corrections to the DC Hamiltonian) to the $1s$ ionization energies have been approximated as the corresponding corrections to the $1s$ orbital energies taken from the calculations by Aucar and collaborators [60]. Finally, the nuclear size effects have been estimated as the difference between the Gaussian nuclear model [65] and the point-like nuclear model.

TABLE II. Kr $1s$ ionization energy in Kr and the Xe $1s$ ionization energy in Xe and $\mathrm{XeF_2}$ (in eV).

	Kr	Xe	$\mathrm{XeF_2}$
Nonrel Koopmans' theorem	14154.4	33317.6	33321.3
Δ [scalar-rel-1e][a]	249.1	1407.2	1407.3
Δ [scalar-rel-2e][b]	9.1	33.0	33.0
Δ [EOM-CCSD]	−49.3	−61.1	−61.3
ΔT	−3.3	−3.8	−3.9
Δ [nuclear size]	−0.3	−2.9	−2.9
Δ [SOC]	−0.3	−2.9	−2.9
Δ [Breit+QED]	−32.7 [60]	−123.4 [60]	−123.4[c]
Δ [Auger shift]	−0.256 [59]	/	/
Total	14326.5	34563.7	34567.2
Experiment	14327.19(13)[d]	34565.13(33)[d]	34567.4(8)[e]

[a] Difference between SFX2C-1e and nonrelativistic.

[b] Difference between SFDC and SFX2C-1e.

[c] Fixed to the atomic value.

[d] Reference [43].

[e] This work.

In the calculations for the $1s \rightarrow np$ Rydberg transitions in Xe and $\mathrm{XeF_2}$, two additional sets of diffuse s-, p-, d-, and f-type functions have been added to the ANO-RCC-unc set for Xe in order to capture the diffuse nature of the Rydberg states [66]. The exponents of the diffuse functions are obtained by multiplying the smallest existing exponents by a factor of 1/3. Since the EOM-CCSDT calculations using such basis sets are not feasible, the triples corrections to the $1s \rightarrow np$ excitation energies have been calculated using the EOM-CCSD with a noniterative treatment of triples contributions [CCSD(T)(a)*] method [67]. For the calculation of the $1s \rightarrow$ LUMO transition in $\mathrm{XeF_2}$, the contributions from the diffuse functions are negligible. Therefore the $1s \rightarrow$ LUMO transition energies at the SFX2C-1e-EOM-CCSD and CCSD(T)(a)*/ANO-RCC-unc levels are reported [68]. All the transition dipole moments and oscillator strengths have been calculated at the SFX2C-1e-CVS-EOM-CCSD level.

Various contributions to the Kr $1s$ ionization energy in Kr and the Xe $1s$ ionization energies in Xe and $\mathrm{XeF_2}$ are summarized in Table II. As expected, the scalar-relativistic effects make significant contributions, 258.2 eV for Kr, 1440.2 eV for Xe, and 1440.3 eV for $\mathrm{XeF_2}$. The one-electron approximation in the SFX2C-1e scheme accounts for 96% of scalar-relativistic effects in the case of Kr and 98% in the case of Xe and $\mathrm{XeF_2}$. In spite of the large absolute values, the scalar-relativistic contributions to $1s$ ionization energies appear to be mainly of atomic character; the corresponding contribution to the relative shift of Xe relative to $\mathrm{XeF_2}$ is only 0.1 eV. The electron correlation and wave function relaxation contributions at the CCSD level are −49.3 eV for Kr, −61.1 eV for Xe, and −61.3 eV for $\mathrm{XeF_2}$. The triples corrections are one order of magnitude smaller and amount to 3 to 4 eV. The contribution of electron correlation and wave-function relaxation to the relative shift of Xe and $\mathrm{XeF_2}$ amounts to 0.3 eV and 10% of the total value, which is greater than the

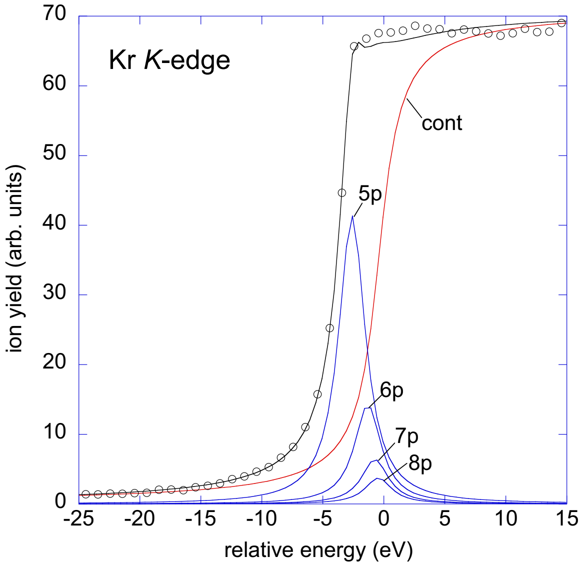

FIG. 4. Model fit to the Kr *K*-edge based on the model in Ref. [15]. The energy scale is relative to the Kr 1*s* ionization energy of 14327.19 (13) eV [43]. The $1s \rightarrow 5p$, $6p$, $7p$, $8p$ Rydberg states and $1s^{-1}$ ionization continuum are indicated. A curve showing the sum of the components is fit to the measured ion yield (open circles).

corresponding scalar-relativistic contribution (0.1 eV). The contributions of the Breit term and the QED effects are rather large in terms of absolute magnitude (−32.7 eV for Kr and −123.4 eV for Xe). Due to the lack of molecular results, we have used the Xe result for XeF_2. This is expected to introduce only small errors, since the contributions from both Breit term and QED effects to 1s ionization energies are rather insensitive to valence occupations, based on results for Kr, Kr^+, and Kr^{2+} [59] and those of I and I^- [69]. For example, the corresponding correction to the Kr 1*s* ionization energy in Kr differs from that in Kr^+ only by 0.1 eV. The SO contributions and the nuclear size effects are relatively small (−0.3 eV for Kr, −2.9 for Xe and XeF_2) but non-negligible.

The experimental determination of the Xe 1*s* ionization energy of XeF_2 and its comparison with the calculations will be discussed in Sec. IV C. Here we focus our discussion on the comparison of the computed Kr 1*s* and Xe 1*s* ionization energies with the experimental values. In these calculations, scalar-relativistic effects have already been rigorously accounted for. Based on the magnitude of the triples contribution (3–4 eV), it seems logical to conclude that the errors of the CVS-EOM-CCSDT results with respect to the treatment of electron correlation and wave function relaxation are below 0.5 eV. Most of the remaining error might lie in the approximate treatment of the corrections due to the Breit term and the QED effects, given the large magnitude of these corrections to the orbital energies. In other words, the treatment of the coupling between electron correlation and the Breit term as well as the QED effects might help to further improve the computational results. In addition, the nuclear size effects of −2.9 eV are only meant to be an estimation of the magnitude. The rigorous treatment requires to account for the inner structure of the nucleus and is beyond the available computational techniques. Based on these analyses, the remaining errors of the computed Xe 1*s* ionization energies can be estimated to be several eV. Therefore, the present agreement of around 2 eV between theory and experiment is reasonably satisfactory.

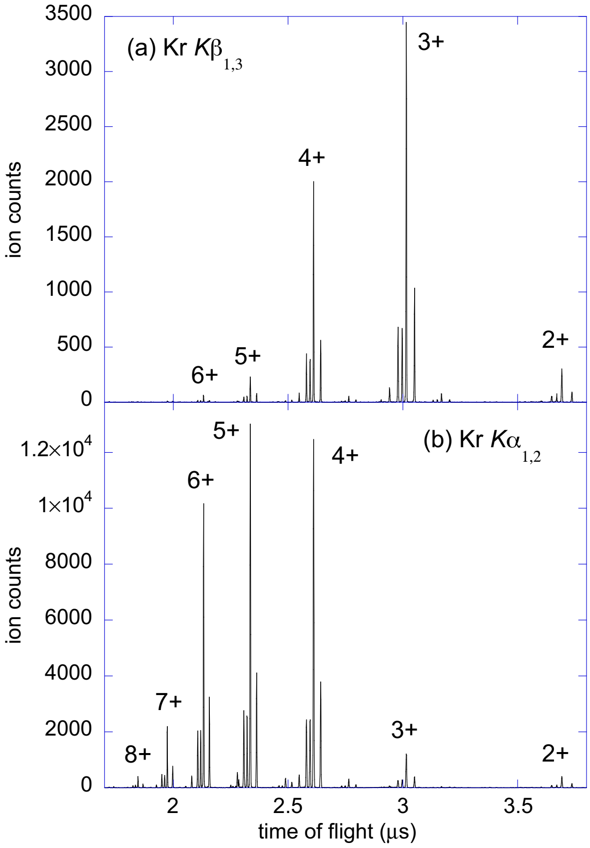

FIG. 5. Ion time of flight spectra of Kr measured in coincidence with (a) $K\beta_{1,3}$ and (b) $K\alpha_{1,2}$ x-ray fluorescence.

IV. RESULTS AND DISCUSSION

A. Kr *K* edge

An ion yield scan across the Kr *K* edge is plotted in Fig. 4 along with a model fit to the $1s \rightarrow 5p$, $6p$, $7p$, $8p$ Rydberg states and the $1s^{-1}$ ionization continuum. Our model reproduces the fit shown in Ref. [15] and accounts for the ~2.7 eV level widths of 1*s*-hole states [18], i.e., the widths of the Lorentzian and arctangent fitting functions. The relative energy scale is referenced to the ionization energy of 14327.19 (13) eV [43]. To investigate effects of the pre-edge resonances, ion TOF spectra were recorded in coincidence with $K\alpha_{1,2}$ and $K\beta_{1,2,3}$ x rays over relative energies of −9 to 3 eV. Sums of the ion TOF spectra are plotted in Fig. 5 and show that the isotopic structure was resolved. The peak widths are 2–5 ns, and the areas of the 82, 83, 84, and 86 Kr-isotopes were determined by peak fitting. Those four isotopes account for >97% of the natural Kr abundance [70]. The $K\beta_2$ x rays, in which the 1*s* hole is transferred to the 4p shell, are unresolved from the $K\beta_{1,3}$ x rays in the SiLi spectrum of Fig. 2. Using the relative intensities listed in Table I, the $K\beta_2$ x rays account for ~9% of the $K\beta_{1,2,3}$ transitions. The $K\beta_2$ transitions only produce Kr^+, because $4p^{-1}$ is the ion ground state and further decays are

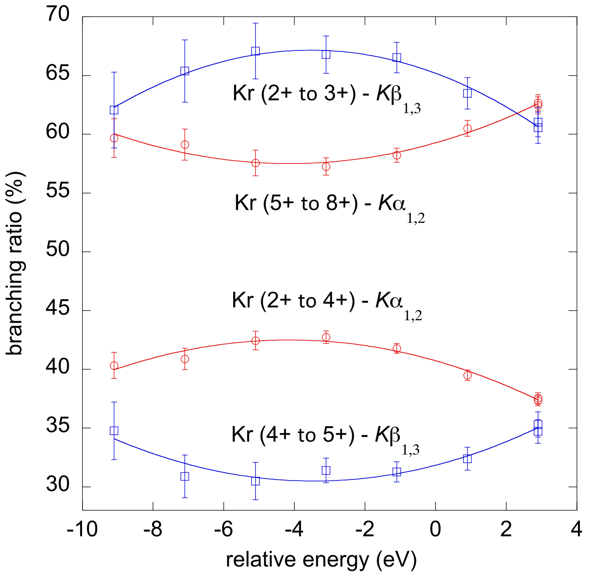

FIG. 6. Kr ion branching ratios measured over the *K*-shell pre-edge and ionization threshold energy range shown in Fig. 4. Circles: sums of branching ratios for Kr ion charge states 2+ to 4+ and 5+ to 8+ measured in coincidence with $K\alpha_{1,2}$ x rays. Squares: sums of branching ratios for Kr ion charge states 2+ to 3+ and 4+ to 5+ measured in coincidence with $K\beta_{1,3}$ x rays. The curves are fits through the measurements to indicate the energy variations. The error bars are statistical uncertainties in the ion charge-state counts.

not possible. The measured average charge states are ∼4.9 for $K\alpha_{1,2}$ x rays and ∼3.2 for $K\beta_{1,2,3}$ x rays in which the initial 1*s* hole is transferred to the 2*p* and 3*p* + 4*p* shells, respectively. For comparison, the calculated average charge states are 4.86 and 3.00 for $L_{2,3}$ and $M_{2,3}$ holes, respectively [71]. Given that $K\beta_{1,3}$ x rays produce $M_{2,3}$ holes with an average charge state of ∼3, in the following we assume that the Kr^+ ions are produced by $K\beta_2$ fluorescence.

Variations of the ion charge state distributions across the pre-edge region are shown in Fig. 6 where sums of branching ratios are plotted. The branching ratios of higher charge states decrease while the lower charge state branching ratios increase. The variations are small but the trends are clear. This effect is attributed to the presence of 5*p*, 6*p*,... spectator electrons produced by photoabsorption in the pre-edge region as suggested by Fig. 4. A qualitative explanation is to assume that spectator electrons have little effect until the end of the cascade decay when they either remain attached to the ion, reducing its charge by one, or undergo a participator-Auger process and produce a low-energy electron. This scenario was examined in detail in two earlier studies of Kr in which a "spectator cascade decay" model was developed [21,22]. The model included estimates of the "sticking probabilities" of the spectator electrons for different Kr ion charge states. The present coincidence experiments select core-hole decays that begin with a radiative transition followed by series of Auger transitions. The assumption that Rydberg electrons retain their quantum numbers in radiative transitions is supported by theoretical treatments of resonant Raman scattering [1,5]. In Auger transitions, however, the Rydberg electrons shake to different levels when the core charge increases [72,73]. We surmise that the sticking probabilities will depend on particular combinations of radiative and Auger cascades.

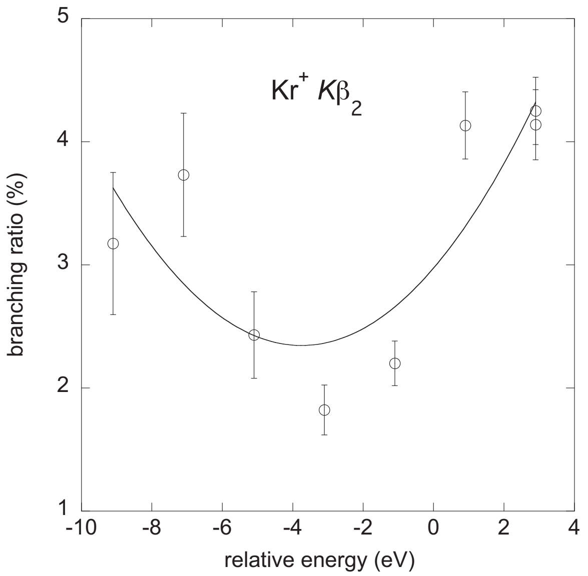

FIG. 7. Kr^+ ion branching ratio measured in coincidence with $K\beta_2$ x rays over the *K*-shell pre-edge and ionization threshold energy range shown in Fig. 4. The curve is a fit to the data to show the energy variation.

In the special case of Kr^+ produced by $K\beta_2$ x-ray emission, the branching ratio decreases in the pre-edge region as shown in Fig. 7. The measurements are noisy due to the small radiative yield, but a dip in the branching ratio is apparent. In this case, spectator electrons that stick to Kr^+ ions produce neutral, metastable states such as $4p^{-1}5p$ that lie below the $4p^{-1}$ ionization threshold and so they deplete the yield of Kr^+

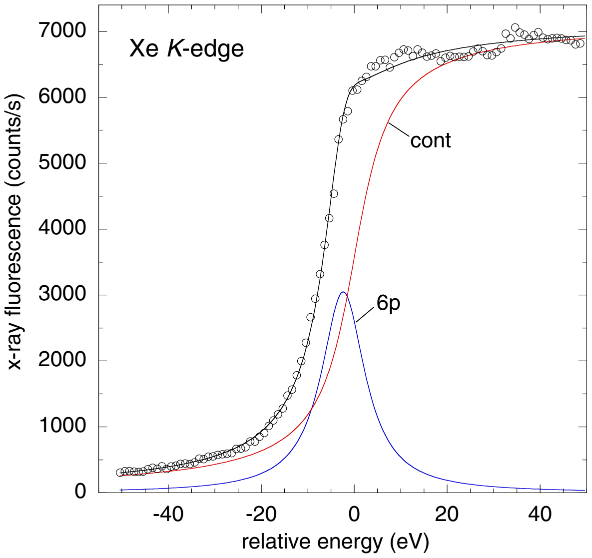

FIG. 8. Model fit to the Xe *K* edge. The energy scale is relative to the Xe 1*s* ionization energy of 34565.13 (33) eV [43]. The $1s \rightarrow 6p$ Rydberg state and $1s^{-1}$ ionization continuum are indicated. A curve showing the sum of the components is fit to the measured x-ray fluorescence rate (open circles).

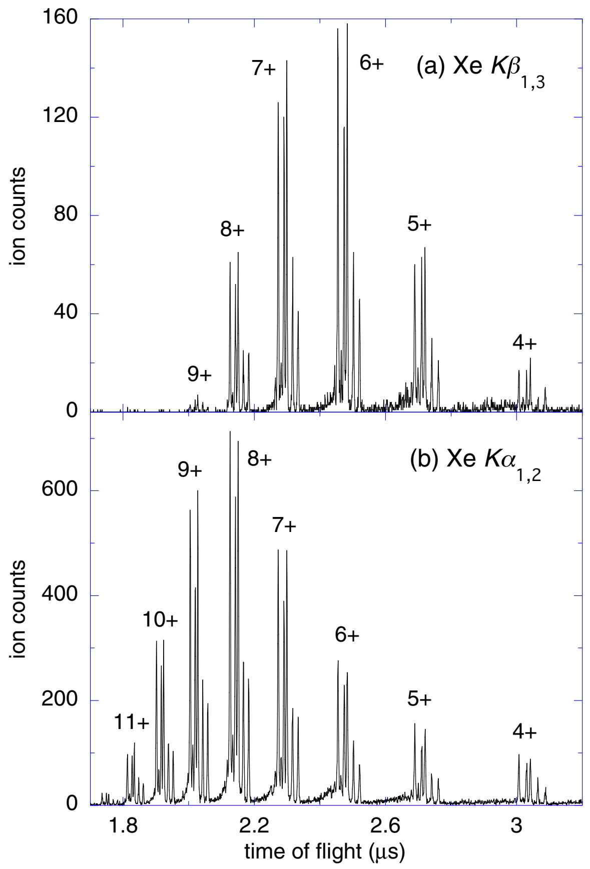

FIG. 9. Ion time of flight spectra of Xe measured in coincidence with (a) $K\beta_{1,3}$ and (b) $K\alpha_{1,2}$ x-ray fluorescence.

ions. Apparently, this process is larger than the addition to the Kr^+ yield produced by spectators sticking to Kr^{2+}.

B. Xe *K* edge

An x-ray fluorescence yield scan across the Xe *K* edge is plotted in Fig. 8 along with a model fit to the $1s \rightarrow 6p$ Rydberg state and the $1s^{-1}$ ionization continuum. Our model follows the analysis of Refs. [16,17] that uses the $Z+1$ approximation [15] and optical data of Cs to place the $1s^{-1}6p$ Rydberg state 2.4 eV below the ionization energy. Due to the large level width of 11.49 eV [18], a single peak is used in the model fit to represent all pre-edge Rydberg states. The relative energy scale is referenced to the ionization energy of 34565.13 (33) eV [43]. Ion TOF spectra were recorded in coincidence with $K\alpha_{1,2}$, $K\beta_{1,3}$, and $K\beta_2$ x-ray fluorescence over relative energies of -13 to 8 eV. The x-ray transitions are resolved in the SiLi spectrum plotted in Fig. 3 and allowed the ion TOF spectra to be filtered on each transition. Sums of the ion TOF spectra are plotted in Fig. 9. The peak widths are 3–4 ns and the isotopic structure [70] was resolved. The areas of each charge state were determined by peak fitting and by summing counts. The average charge states are ∼8.0 for $K\alpha_{1,2}$, ∼6.2 for $K\beta_{1,3}$, and ∼3.6 for $K\beta_2$ transitions, in which the initial $1s$ hole is transferred to the 2p, 3p, and 4p shells, respectively. For comparison, the calculated average charge states are 7.75, 6.57, and 3.02 for $L_{2,3}$, $M_{2,3}$, and $N_{2,3}$ holes, respectively [74].

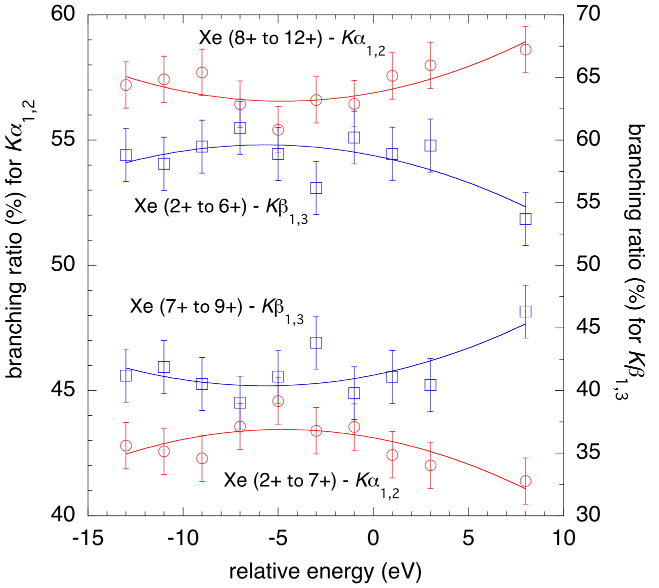

FIG. 10. Xe ion branching ratios measured over the *K*-shell pre-edge and ionization threshold energy range shown in Fig. 8. Circles and left vertical axis: sums of branching ratios for Xe ion charge states 2+ to 7+ and 8+ to 12+ measured in coincidence with $K\alpha_{1,2}$ x rays. Squares and right vertical axis: sums of branching ratios for Xe charge states 2+ to 6+ and 7+ to 9+ measured in coincidence with $K\beta_{1,3}$ x rays. The curves are fits through the measurements to indicate the energy variations. The error bars are statistical uncertainties in the ion charge-state counts.

Small variations of ion charge state branching ratios across the pre-edge and continuum threshold region are observed and plotted in Fig. 10. Sums of branching ratios are plotted to reduce scatter. The trends are the same as observed for Kr in Fig. 6, i.e., the lower charge states increase in the pre-edge region while higher charge states decrease. In both cases, the effects are attributed to spectator electrons generated by $1s \rightarrow np$ resonant x-ray absorption. Not shown are results for the weak $K\beta_2$ channel that primarily generates Xe^{3+} and Xe^{4+}. The Xe^{3+} yield shows a small maximum and the Xe^{4+} yield shows a small minimum across the -13 to 8 eV energy range in accord with the trends plotted in Fig. 10.

Comparing Figs. 6 and 10, the charge-state variations in Xe are smaller and less distinct than in Kr. The larger level width of a Xe $1s$ hole increases the overlap between Rydberg states and the continuum and reduces the contrast between hole decays with and without spectator electrons. Also, more Auger decay steps occur in Xe due to the increased number of outer shell electrons. This results in a larger number of charge states and more complicated cascades involving spectators in which charge states gain or lose population. To explore this topic further, theoretical calculations of the Auger cascade would be informative, such as applied to the cases of Xe $3d$ ionization [75] and Xe $3d \rightarrow 6p$ resonant excitation [76].

C. Xe *K* edge of XeF_2

Although Xe is a closed-shell atom, the high electron affinity of F induces bond formation in linear F–Xe–F by charge sharing among the $2p_z$ orbitals of the F atoms and

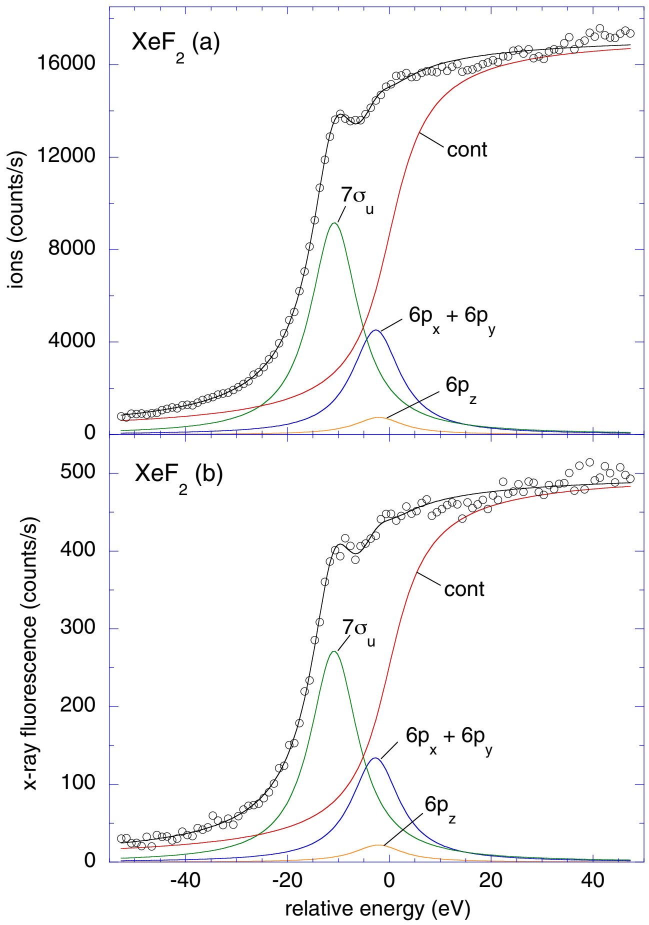

FIG. 11. Model fits to the Xe *K* edge of XeF_2 using (a) ion yield and (b) x-ray fluorescence yield. The energy scale is relative to the $1s$ ionization energy of 34567.4 (8) eV. The components are the $1s \rightarrow 7\sigma_u$ lowest unoccupied molecular orbital (LUMO), the $1s \rightarrow 6p_x + 6p_y$ and $1s \rightarrow 6p_z$ Rydberg states, and the $1s^{-1}$ ionization continuum. Curves showing the sums of the components are fit to the measured yields (open circles).

the $5p_z$ orbital of Xe, where z is taken along the molecular axis [77–79]. The valence atomic orbitals interact to form the bonding, nonbonding, and antibonding molecular orbitals, while the core levels remain localized [79]. Several spectroscopic studies have been made in various energy ranges that compare transition energies and transition strengths of Xe and XeF_2. The Xe $4d$, Xe $3d$, and F $1s$ ionization energies are sensitive to the shielding effects of valence electron charge distributions, i.e., "chemical shifts" [80–82]. Also, an intense, antibonding $7\sigma_u$ lowest unoccupied molecular orbital (LUMO) [79] is observed in vacuum-ultraviolet [78,83], far-ultraviolet [84], and soft x-ray [45] photoabsorption spectra of XeF_2. Here we report on the Xe $1s$ chemical shift and observation of the LUMO in the Xe *K*-edge spectrum of XeF_2.

Our fit to the *K* edge of atomic Xe is shown in Fig. 8 and our fits to the Xe *K* edge of XeF_2 are shown in Fig. 11. The ion yield and fluorescence yield were recorded in the same scan and gave similar fitted results. The fits were guided by the calculated energies and oscillator strengths of the $6p$ Rydberg states and LUMO listed in Table III. Our calculations show that the $1s^{-1}6p_z$ state is strongly perturbed by the presence of the $7\sigma_u$ LUMO. The fits were constrained by requiring a $6p_z$ Lorentzian 2.1 eV below the $1s^{-1}$ continuum edge, a $6p_x + 6p_y$ Lorenzian 2.7 eV below the edge, and their amplitudes to be in the ratio of the oscillator strengths listed in Table III. A third Lorentzian represented the LUMO and an arctangent function modeled the $1s^{-1}$ edge. All functions used level widths of 11.49 eV. The fits yielded the positions of the LUMO and the $1s^{-1}$ ionization energy and the relative amplitudes of the $6p_x$, $6p_y$, $6p_z$, and LUMO. The Xe and XeF_2 edge scans were recorded sequentially with the same x-ray energies. From the fits in Figs. 8 and 11, the $1s^{-1}$ energy of XeF_2 is 2.3 (5) eV higher than in atomic Xe. This shift is similar to the chemical shift of 2.87 (2) eV for the Xe $3d_{5/2}$ binding energy of Xe reported in Ref. [80]. Adding 2.3 (5) eV to the Xe $1s$ binding energy [43] gives 34567.4 (8) eV for XeF_2. The experimental shift of 2.3 (5) eV is a little less than the calculated shift of 3.5 eV in Table II. The fits locate the LUMO at 10.8 (4) eV below the $1s^{-1}$ edge compared with 9.8 eV from the calculations. From the fit, the sum of the amplitudes of the $6p_x$, $6p_y$, and $6p_z$ components is 0.58 times the LUMO amplitude compared with 0.25 for the ratio of the calculated oscillator strengths. However, given the simplifying assumptions made in the fits, we do not consider the derived results to be definitive, but they do give a qualitative picture of the edge structure.

D. Ion fragmentation of XeF_2

As suggested by the illustration in Fig. 1 and reported in previous experiments on XeF_2 [23,45,46], core-hole decays following inner-shell photoionization of the Xe atom lead to charge production on the F atoms and dissociation into energetic atomic ions, i.e., a Coulomb explosion [85]. While the ion TOF spectra of atomic Kr and Xe in Figs. 5 and 9 appear as narrow peaks with resolved isotopic structure, the TOF peaks of F^{q+} ($q = 1$–4) in Fig. 12 are broadened by the energies they are ejected with when the molecular ion

TABLE III. Calculated energies and oscillator strengths of Xe $1s \rightarrow 6p_x$, $6p_y$, $6p_z$, and LUMO transitions in XeF_2. Energies are relative to the $1s^{-1}$ ionization energy. Results of the fits plotted in Fig. 11 are given for comparison.

Transition	ΔE (eV) (theory)	Oscillator strength (a.u.)	ΔE (eV) (fit)	Amplitude (fit)
$6p_x$	−2.7	0.0000787	−2.7[a]	0.25 (2)
$6p_y$	−2.7	0.0000787	−2.7[a]	0.25 (2)
$6p_z$	−2.1	0.0000257	−2.1[a]	0.08 (1)
LUMO	−9.8	0.0007445	−10.8 (4)	1.00 (3)

[a] Fixed to theory.

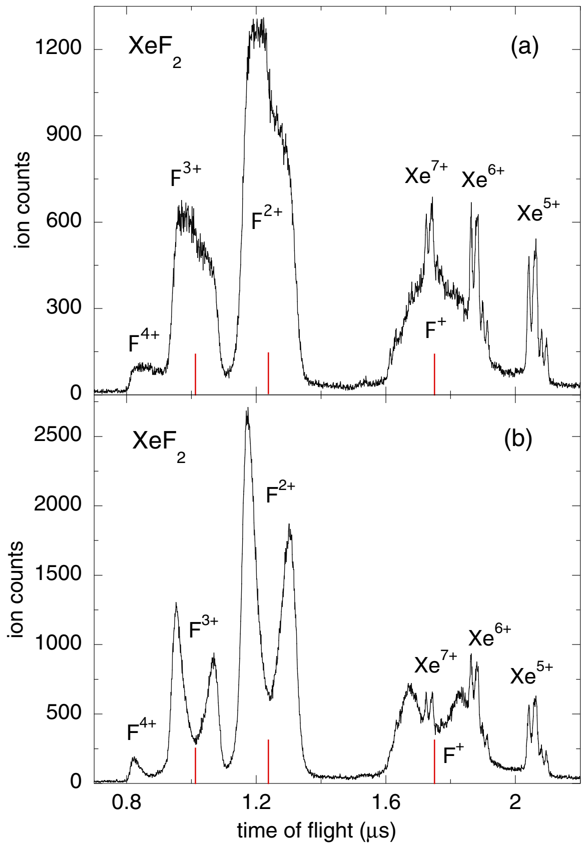

FIG. 12. Ion time of flight spectra of XeF$_2$ measured in coincidence with $K\alpha_{1,2}$ x rays. (a) Recorded in the ionization continuum at 34577 eV. The F ion peaks are broadened by energetic fragmentation. (b) Recorded on the $7\sigma_u$ resonance at 34557 eV. The F ion peaks are broadened by energetic fragmentation and split due to molecular alignment by resonant photoabsorption. The markers show the calculated times of flight of F ions having zero velocity components along the flight axis.

dissociates. Figure 12 compares ion TOF spectra recorded above the Xe 1s ionization edge with spectra recorded on the $7\sigma_u$ resonance. The F ion peaks are broadened in both spectra but are clearly split into two components for $7\sigma_u$ excitation due to spatial alignment of XeF$_2$ molecules selected by resonant photoabsorption. The components with smaller TOFs are ions ejected toward the detector and arrive before the ions ejected away from the detector. F ions ejected away from the detector turn around in the extraction field and pass through the gas jet. Those ions experience a greater number of collisions with the background gas than do the ions ejected toward the detector.

We attribute the asymmetries in the amplitudes of the two components of each charge state to the fact that the faster component is more likely to be detected in the first hit and partly to the effect of charge exchange from ion-gas collisions [86]. A similar asymmetry is seen in the F ion peaks measured above the ionization edge. However, here we focus on using the TOF splittings between the faster and slower components measured on resonance to determine the fragmentation energies of the F ions.

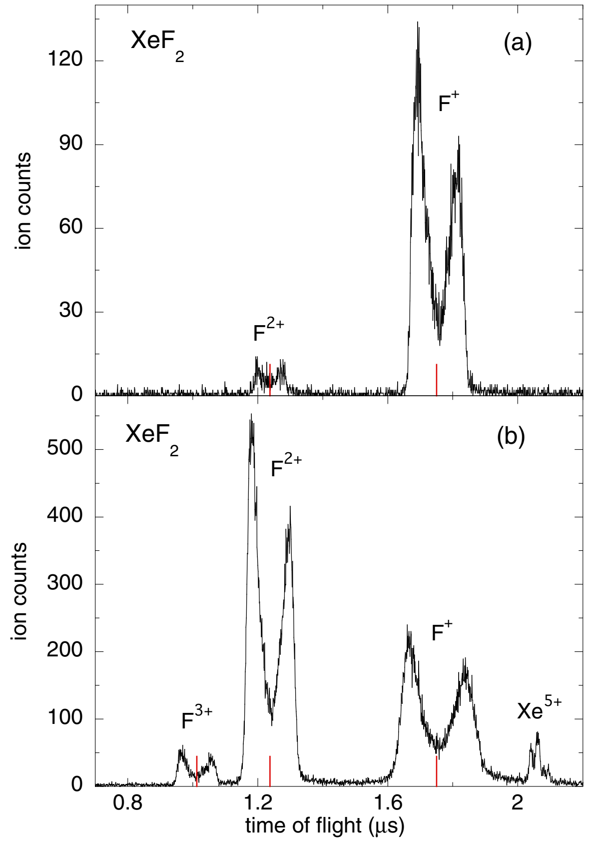

FIG. 13. Ion time of flight spectra of XeF$_2$ measured on the $7\sigma_u$ resonance at 34557 eV in coincidence with (a) $K\beta_2$ x rays and (b) $K\beta_{1,3}$ x rays. The markers show the calculated times of flight of F ions having zero velocity components along the flight axis.

The flight axis of the ion TOF instrument was positioned parallel to the linear polarization direction of the x-ray beam, and the transition moment of the $1s \rightarrow 7\sigma_u$ resonance is parallel to the molecular axis. Resonant photoabsorption selects a $\cos^2\theta$ distribution of molecular axes with respect to the polarization direction and ion flight axis, and we assume that the F ions are ejected along the directions of the molecular axes. The geometry, electric fields, and detector of the instrument are designed to collect and detect energetic ions. Ions ejected forward and backward at $\theta = 0^\circ$ have the largest TOF splittings, while ions ejected at 90° have the same TOFs but strike the detector at different radial positions.

The ions are created in a static electric field that accelerates the ions toward the detector. Ions ejected away from the detector are slowed to zero in the field, turn around and regain their initial energy when they reach the starting point. From the starting point, their TOFs are the same as those ions with the same initial energy that were ejected toward the detector. For the $\theta = 0^\circ$ case of an ion of mass m (amu), charge q, electric field E_s (V/cm), and initial energy U_0 (eV), the time to turn around and return to the starting point is [89]

$$\Delta T(\text{ns}) = (1018)(2/qE_s)(2mU_0)^{1/2}, \qquad (1)$$

where 1018 ns/cm is a units conversion factor. For the present case of a $\cos^2\theta$ distribution of molecular axes, it is the z components of the ion momenta that result in nonzero

TABLE IV. Energies of Xe hole states, average charge states Xe-$\bar{q}$ from hole decays in atomic Xe, average charge states F-$\bar{q}$ and kinetic energies of F^{q+} ions from corresponding hole decays in XeF_2 molecules. Xe-$\bar{q}$ theory: Ref. [74]; expt: this work.

Xe hole	Energy (eV)	Xe-$\bar{q}$ (theory)	Xe-$\bar{q}$ (expt)	F-$\bar{q}$	F^+ (eV)	F^{2+} (eV)	F^{3+} (eV)	F^{4+} (eV)
2*p*	4889	7.75	7.3 (1)	2.0 (2)	28 (17)	53 (25)	91 (43)	157 (16)
3*p*	958	6.57	6.4 (2)	1.7 (4)	25 (12)	40 (18)	61 (27)	–
4*p*	146	3.02	3.4 (2)	1.0 (1)	12 (5)	–	–	–

turn-around times. Since the average *z* component is 3/4 of the total momentum, it follows that the ion energy is related to the average turn-around time by

$$U_0(eV) = [(4/3)(\Delta T q E_s)/(1018)]^2/8m, \tag{2}$$

where ΔT is the splitting between the centroids of the faster and slower components. The TOFs of the Xe and F ions were accurately calculated (±1 ns) by simulating the geometry and electric fields of the instrument. This allows the use of Eq. (2) to determine fragmentation energies from the TOF splittings. The markers in Fig. 12 are the calculated TOFs for F ions created with zero velocity components along the flight axis and closely match the midpoints of the peaks.

Figure 12(b) shows the TOF spectrum recorded on resonance in coincidence with $K\alpha_{1,2}$ x rays, and Fig. 13 shows the on-resonance TOFs in coincidence with $K\beta_{1,3}$ and $K\beta_2$ x rays. Two effects are apparent from the figures—the amplitudes of the higher charge states are reduced and the peak splittings decrease as the initial 1*s* hole is transferred to the 2*p*, 3*p*, and 4*p* shells, leaving less energy in the system and fewer outer electrons to participate in subsequent Auger decays. The centroids and standard deviations of the faster and slower components of each charge state were determined by peak fitting. The F^+ peak in Fig. 12(b) is overlapped by Xe^{6+}, Xe^{7+}, and Xe^{8+}. The isotopic structures of the Xe peaks were determined by fitting a TOF spectrum of atomic Xe and were included in fits to the F^+ peak. Using Eq. (2), the F ion energies determined from the TOF splittings are listed in Table IV. For comparison, the table includes the energies of Xe 2*p*, 3*p*, and 4*p* holes, the calculated average charge states for decays of Xe holes [74], and the average charge states for atomic Xe measured concurrently with XeF_2. The present results for F^+, F^{2+}, and F^{3+} energies measured in coincidence with $K\alpha_{1,2}$ x rays agree with previous measurements using the same method [23], but the F^{4+} energy determined here is somewhat higher. It was noted in Ref. [23] that the measured ion energies are smaller than Coulomb energies calculated at the ground state geometry of XeF_2. This suggests that the molecular ion begins to dissociate while charges on the atomic sites are still developing. The present results also show how the F ion energies and charge-state distributions vary as the initial 1*s* hole is transferred radiatively to three outer shells. While the trends are not surprising, the measurements provide an example of how charge and energy are transferred to molecular ion fragmentation for different core hole decay pathways.

V. CONCLUSION

One of the goals of this work was to demonstrate that the effects of pre-edge resonances in the *K*-shell x-ray absorption spectra of heavy atoms can be observed in core-hole decay measurements. This was achieved by measuring small but distinct variations of ion charge-state distributions in Kr and Xe resulting from the presence of spectator electrons. In XeF_2, excitation of the lowest unoccupied molecular orbital below the Xe *K* edge selects spatially aligned molecules. Their core-hole decays lead to energetic ion fragmentation, and the alignment produces splittings in ion time of flight peaks that were used to determine ion energies. The experiments exploit x-ray/ion coincidence methods that select core-hole decay processes that begin with transfers of initial 1*s* holes to 2*p*, 3*p*, or 4*p* shells. This provides more information on the decay processes, but the ion yield measurements still average over many unobserved decay steps. More selective coincidence measurements, perhaps by combining x-ray and electron spectroscopies, would provide more detailed information.

We also report a computational study based on relativistic core-valence-separated equation-of-motion coupled-cluster methods that features rigorous and systematic treatment of scalar-relativistic, electron-correlation, and wave function-relaxation effects as well as a thorough investigation of various relativistic contributions. The computational results have been shown to give excellent agreement with measured *K*-shell ionization energies in heavy elements that require accurate treatment of relativistic effects and electron-electron interactions. The calculated energies and oscillator strengths on the $1s^{-1}7\sigma_u$ LUMO and $1s^{-1}6p$ Rydberg states have also played a useful role in providing guidance to a model fit of the pre-edge structure in the Xe *K* edge of XeF_2. These computational methods appear to be quite promising for future applications to x-ray and inner-shell processes in molecules.

ACKNOWLEDGMENTS

This work was supported by the US Department of Energy, Office of Science, Basic Energy Sciences, Chemical Sciences, Geosciences, and Biosciences Division. This research used resources of the Advanced Photon Source, a US Department of Energy (DOE) Office of Science User Facility operated for the DOE Office of Science by Argonne National Laboratory under Contract No. DE-AC02-06CH11357.

[1] T. Åberg and B. Crasemann, in *Resonant Anomalous X-ray Scattering: Theory and Applications*, edited by G. Materlik, C. J. Sparks, and K. Fischer (North-Holland, Amsterdam, 1994), p. 431.

[2] F. Gel'mukhanov and H. Ågren, Phys. Rep. **312**, 87 (1999).

[3] G. B. Armen, H. Aksela, T. Åberg, and S. Aksela, J. Phys. B **33**, R49 (2000).

[4] M. N. Piancastelli, J. Electron Spectrosc. Relat. Phenom. **107**, 1 (2000).

[5] J. C. Levin and G. B. Armen, Radiat. Phys. Chem. **70**, 105 (2004).

[6] A. Russek and W. Mehlhorn, J. Phys. B **19**, 911 (1986).

[7] W. Eberhardt, S. Bernstorff, H. W. Jochims, S. B. Whitfield, and B. Crasemann, Phys. Rev. A **38**, 3808 (1988).

[8] J. Tulkki, T. Åberg, S. B. Whitfield, and B. Crasemann, Phys. Rev. A **41**, 181 (1990).

[9] M. Žitnik, M. Kavčič, K. Bučar, A. Mihelič, M. Štuhec, J. Kokalj, and J. Szlachetko, Phys. Rev. A **76**, 032506 (2007).

[10] L. El Khoury, L. Journel, R. Guillemin, S. Carniato, W. C. Stolte, T. Marin, D. W. Lindle, and M. Simon, J. Chem. Phys. **136**, 024319 (2012).

[11] J.-E. Rubensson, J. Söderström, C. Binggeli, J. Gråsjö, J. Andersson, C. Såthe, F. Hennies, V. Bisogni, Y. Huang, P. Olalde, T. Schmitt, V. N. Strocov, A. Föhlisch, B. Kennedy, and A. Pietzsch, Phys. Rev. Lett. **114**, 133001 (2015).

[12] P. Glatzel and U. Bergmann, Coord. Chem. Rev. **249**, 65 (2005).

[13] L. J. P. Ament, M. van Veenendaal, T. P. Devereaux, J. P. Hill, and J. van den Brink, Rev. Mod. Phys. **83**, 705 (2011).

[14] M. Coreno, L. Avaldi, R. Camilloni, K. C. Prince, M. de Simone, J. Karvonen, R. Colle, and S. Simonucci, Phys. Rev. A **59**, 2494 (1999).

[15] M. Breinig, M. H. Chen, G. E. Ice, F. Parente, B. Crasemann, and G. S. Brown, Phys. Rev. A **22**, 520 (1980).

[16] M. Deutsch, G. Brill, and P. Kizler, Phys. Rev. A **43**, 2591 (1991).

[17] M. Deutsch and P. Kizler, Phys. Rev. A **45**, 2112 (1992).

[18] M. H. Chen, B. Crasemann, and H. Mark, Phys. Rev. A **21**, 436 (1980).

[19] P. Glatzel, T.-C. Weng, K. Kvashnina, J. Swarbrick, M. Sikora, E. Gallo, N. Smolentsev, and R. Alonso-Mori, J. Electron Spectrosc. Relat. Phenom. **188**, 17 (2013).

[20] R. Guillemin, K. Jänkälä, B. C. de Miranda, T. Marin, L. Journel, T. Marchenko, O. Travnikova, G. Goldsztejn, I. Ismail, R. Püttner, D. Céolin, B. Lassalle-Kaiser, M. N. Piancastelli, and M. Simon, Phys. Rev. A **97**, 013418 (2018).

[21] G. B. Armen, E. P. Kanter, B. Krässig, J. C. Levin, S. H. Southworth, and L. Young, Phys. Rev. A **67**, 042718 (2003).

[22] G. B. Armen, E. P. Kanter, B. Krässig, J. C. Levin, S. H. Southworth, and L. Young, Phys. Rev. A **69**, 062710 (2004).

[23] R. W. Dunford, S. H. Southworth, D. Ray, E. P. Kanter, B. Krässig, L. Young, D. A. Arms, E. M. Dufresne, D. A. Walko, O. Vendrell, S.-K. Son, and R. Santra, Phys. Rev. A **86**, 033401 (2012).

[24] S. Corde, A. Joubert, J. F. Adam, A. M. Charvet, J. F. L. Bas, F. Estève, H. Elleaume, and J. Balosso, Br. J. Cancer **91**, 544 (2004).

[25] R. F. Martin and L. E. Feinendegen, Intl. J. Radiat. Bio. **92**, 617 (2016).

[26] L. Young, E. P. Kanter, B. Krässig, Y. Li, A. M. March, S. T. Pratt, R. Santra, S. H. Southworth, N. Rohringer, L. F. DiMauro, G. Doumy, C. A. Roedig, N. Berrah, L. Fang, M. Hoener, P. H. Bucksbaum, J. P. Cryan, S. Ghimire, J. M. Glownia, D. A. Reis, J. D. Bozek, C. Bostedt, and M. Messerschmidt, Nature (London) **466**, 56 (2010).

[27] R. Boll, B. Erk, R. Coffee, S. Trippel, T. Kierspel, C. Bomme, J. D. Bozek, M. Burkett, S. Carron, K. R. Ferguson, L. Foucar, J. Küpper, T. Marchenko, C. Miron, M. Patanen, T. Osipov, S. Schorb, M. Simon, M. Swiggers, S. Techert, K. Ueda, C. Bostedt, D. Rolles, and A. Rudenko, Struct. Dyn. **3**, 043207 (2016).

[28] A. Rudenko, L. Inhester, K. Hanasaki, X. Li, S. J. Robatjazi, B. Erk, R. Boll, K. Toyota, Y. Hao, O. Vendrell, C. Bomme, E. Savelyev, B. Rudek, L. Foucar, S. H. Southworth, C. S. Lehmann, B. Kraessig, T. Marchenko, M. Simon, K. Ueda, K. R. Ferguson, M. Bucher, T. Gorkhover, S. Carron, R. Alonso-Mori, J. E. Koglin, J. Correa, G. J. Williams, S. Boutet, L. Young, C. Bostedt, S.-K. Son, R. Santra, and D. Rolles, Nature (London) **546**, 129 (2017).

[29] B. Rudek, K. Toyota, L. Foucar, B. Erk, R. Boll, C. Bomme, J. Correa, S. Carron, S. Boutet, G. J. Williams, K. R. Ferguson, R. Alonso-Mori, J. E. Koglin, T. Gorkhover, M. Bucher, C. S. Lehmann, B. Krässig, S. H. Southworth, L. Young, C. Bostedt, K. Ueda, T. Marchenko, M. Simon, Z. Jurek, R. Santra, A. Rudenko, S.-K. Son, and D. Rolles, Nat. Commun. **9**, 4200 (2018).

[30] P. J. Ho, E. P. Kanter, and L. Young, Phys. Rev. A **92**, 063430 (2015).

[31] K. Toyota, S.-K. Son, and R. Santra, Phys. Rev. A **95**, 043412 (2017).

[32] P. Norman and A. Dreuw, Chem. Rev. **118**, 7208 (2018).

[33] H. Koch, H. J. Aa. Jensen, P. Jørgensen, and T. Helgaker, J. Chem. Phys. **93**, 3345 (1990).

[34] G. D. Purvis III and R. J. Bartlett, J. Chem. Phys. **76**, 1910 (1982).

[35] K. Kowalski and P. Piecuch, J. Chem. Phys. **115**, 643 (2001).

[36] S. A. Kucharski, M. Wlock, M. Musial, and R. J. Bartlett, J. Chem. Phys. **115**, 8263 (2001).

[37] A. I. Krylov, Annu. Rev. Phys. Chem. **59**, 433 (2008).

[38] L. S. Cederbaum, W. Domcke, and J. Schirmer, Phys. Rev. A **22**, 206 (1980).

[39] S. Coriani and H. Koch, J. Chem. Phys. **143**, 181103 (2015).

[40] J. Liu., D. Matthews, S. Coriani, and L. Cheng, J. Chem. Theory Comp. **15**, 1642 (2019).

[41] K. G. Dyall and K. Fægri, *Introduction to Relativistic Quantum Chemistry* (Oxford University Press, New York, 2007), Part III.

[42] D. A. Walko, B. W. Adams, G. Doumy, E. M. Dufresne, Y. Li, A. M. March, A. R. Sandy, J. Wang, H. Wen, and Y. Zhu, in *Proceedings of the 12th International Conference on Synchrotron Radiation Instrumentation – SRI2015*, edited by Q. Shen and C. Nelson, AIP Conf. Proc. No. 1741 (AIP, New York, 2016), p. 030048.

[43] R. D. Deslattes, E. G. Kessler, Jr., P. Indelicato, L. de Billy, E. Lindroth, and J. Anton, Rev. Mod. Phys. **75**, 35 (2003).

[44] J. B. Kortright and A. C. Thompson, in *X-Ray Data Booklet*, 3rd ed. (Lawrence Berkeley National Laboratory, University of California, Berkeley, 2009).

[45] S. H. Southworth, R. Wehlitz, A. Picón, C. S. Lehmann, L. Cheng, and J. F. Stanton, J. Chem. Phys. **142**, 224302 (2015).

[46] A. Picón, C. S. Lehmann, C. Bostedt, A. Rudenko, A. Marinelli, T. Osipov, D. Rolles, N. Berrah, C. Bomme, M. Bucher, G. Doumy, B. Erk, K. R. Ferguson, T. Gorkhover, P. J. Ho, E. P. Kanter, B. Krässig, J. Krzywinski, A. A. Lutman, A. M. March, D. Moonshiram, D. Ray, L. Young, S. T. Pratt, and S. H. Southworth, Nat. Commun. **7**, 11652 (2016).

[47] D. A. Matthews and J. F. Stanton, J. Chem. Phys. **142**, 064108 (2015).

[48] J. H. Baraban, D. A. Matthews, and J. F. Stanton, J. Chem. Phys. **144**, 111102 (2016).

[49] CFOUR, Coupled-Cluster techniques for Computational Chemistry, a quantum-chemical program package by J. F. Stanton, J. Gauss, L. Cheng, M. E. Harding, D. A. Matthews, P. G. Szalay with contributions from A. A. Auer, R. J. Bartlett, U. Benedikt, C. Berger, D. E. Bernholdt, Y. J. Bomble, O. Christiansen, F. Engel, R. Faber, M. Heckert, O. Heun, M. Hilgenberg, C. Huber, T.-C. Jagau, D. Jonsson, J. Jusélius, T. Kirsch, K. Klein, W. J. Lauderdale, F. Lipparini, T. Metzroth, L. A. Mück, D. P. O'Neill, D. R. Price, E. Prochnow, C. Puzzarini, K. Ruud, F. Schiffmann, W. Schwalbach, C. Simmons, S. Stopkowicz, A. Tajti, J. Vázquez, F. Wang, J. D. Watts and the integral packages MOLECULE (J. Almlöf and P. R. Taylor), PROPS (P. R. Taylor), ABACUS (T. Helgaker, H. J. Aa. Jensen, P. Jørgensen, and J. Olsen), and ECP routines by A. V. Mitin and C. van Wüllen. For the current version, see http://www.cfour.de.

[50] K. G. Dyall, J. Chem. Phys. **100**, 2118 (1994).

[51] K. G. Dyall, J. Chem. Phys. **115**, 9136 (2001).

[52] K. G. Dyall, J. Chem. Phys. **106**, 9618 (1997).

[53] W. Kutzelnigg and W. Liu, J. Chem. Phys. **123**, 241102 (2005).

[54] M Iliaś and T. Saue, J. Chem. Phys. **126**, 064102 (2007).

[55] W. Liu and D. Peng, J. Chem. Phys. **131**, 031104 (2009).

[56] C. van Wüllen and C. Michauk, J. Chem. Phys. **123**, 204113 (2005).

[57] L. Cheng and J. Gauss, J. Chem. Phys. **134**, 244112 (2011).

[58] L. Cheng and J. Gauss, J. Chem. Phys. **135**, 084114 (2011).

[59] L. Pan, D. R. Beck, and S. M. O'Malley, J. Phys. B **38**, 3721 (2005).

[60] K. Koziol and G. A. Aucar, J. Chem. Phys. **148**, 134101 (2018).

[61] K. Fægri, Jr., Theor. Chem. Acc. **105**, 252 (2001).

[62] B. O. Roos, V. Veryazov, and P. Wildmark, Theor. Chem. Acc. **111**, 345 (2004).

[63] T. H. Dunning, Jr., J. Chem. Phys. **90**, 1007 (1989).

[64] J. Liu and L. Cheng, J. Chem. Phys. **148**, 144108 (2018).

[65] L. Visscher and K. G. Dyall, At. Data Nucl. Data Tables **67**, 207 (1997).

[66] The excitation energies obtained using one and two sets of diffuse functions differ by less than 0.01 eV.

[67] D. A. Matthews and J. F. Stanton, J. Chem. Phys. **145**, 124102 (2016).

[68] The difference between the EOM-CCSDT and EOM-CCSD(T)(a)* results for the relative shift of the Xe 1s to LUMO excitation energies with respect to the Xe 1s ionization energies have been estimated using atomic natural orbital basis of triple-zeta quality recontracted for the SFX2C-1e scheme (these basis sets are available on http://www.cfour.de). The values amount to only around 0.1 eV, and thus have only minor effects on the present analysis.

[69] N. Boudjemia, K. Jänkälä, T. Gejo, K. Nagaya, K. Tamasaku, M. Huttula, M. N. Piancastelli, M. Simon, and M. Oura, Phys. Chem. Chem. Phys. **21**, 5448 (2019).

[70] M. Berglund and M. E. Wieser, Pure Appl. Chem. **83**, 397 (2011).

[71] A. G. Kochur, V. L. Sukhorukov, A. I. Dudenko, and Ph. V. Demekhin, J. Phys. B. **28**, 387 (1995).

[72] S. B. Whitfield, J. Tulkki, and T. Åberg, Phys. Rev. A **44**, R6983 (1991).

[73] G. B. Armen, J. Phys. B **29**, 677 (1996).

[74] A. G. Kochur, A. I. Dudenko, V. L. Sukhorukov, and I. D. Petrov, J. Phys. B **27**, 1709 (1994).

[75] V. Jonauskas, L. Partanen, S. Kučas, R. Karazija, M. Huttula, S. Aksela, and H. Aksela, J. Phys. B **36**, 4403 (2003).

[76] L. Partanen, R. Sankari, S. Osmekhin, Z. F. Hu, E. Kukk, and H. Aksela, J. Phys. B **38**, 1881 (2005).

[77] R. E. Rundle, J. Am. Chem. Soc. **85**, 1112 (1963).

[78] E. G. Wilson, J. Jortner, and S. A. Rice, J. Am. Chem. Soc. **85**, 813 (1963).

[79] H. Basch, J. W. Moskowitz, C. Hollister, and D. Hankin, J. Chem. Phys. **55**, 1922 (1971).

[80] T. X. Carroll, R. W. Shaw, Jr., T. D. Thomas, C. Kindle, and N. Bartlett, J. Am. Chem. Soc. **96**, 1989 (1974).

[81] G. M. Bancroft, P.-Å. Malmquist, S. Svensson, E. Basilier, U. Gelius, and K. Siegbahn, Inorg. Chem. **17**, 1595 (1978).

[82] J. N. Cutler, G. M. Bancroft, J. D. Bozek, K. H. Tan, and G. J. Schrobilgen, J. Am. Chem. Soc. **113**, 9125 (1991).

[83] U. Nielsen and W. H. E. Schwarz, Chem. Phys. **13**, 195 (1976).

[84] F. J. Comes, R. Haensel, U. Nielsen, and W. H. E. Schwarz, J. Chem. Phys. **58**, 516 (1973).

[85] Z. Vager, R. Naaman, and E. P. Kanter, Science **244**, 426 (1989).

[86] The most likely process in the relatively slow collisions of F ions with background gas is electron capture. To estimate this effect we use cross sections from an empirical scaling law developed by Müller and Salzborn [87]. As an example, the cross section for a F^{2+} ion to capture one electron from XeF_2 molecules at low energy is $\sim 3 \times 10^{-15}$ cm^2, where we used an ionization potential of 12.5 eV for XeF_2 [88]. If the target thickness (gas density times path length back and forth through the gas jet) for an ion ejected away from the detector was 3.3×10^{13} cm^{-2}, there would be a 10% probability for an F^{2+} ion to be converted to F^+ within the jet. Ions ejected towards the detector would be less affected. We conclude that charge exchange effects could contribute to the observed asymmetries of the F ion peaks.

[87] A. Müller and E. Salzborn, Phys. Lett. **62A**, 391 (1977).

[88] C. R. Brundle, M. B. Robin, and G. R. Jones, J. Chem. Phys. **52**, 3383 (1970).

[89] W. C. Wiley and I. H. McLaren, Rev. Sci. Instrum. **26**, 1150 (1955).